Electronic Supplementary Information

Exploring the potential of transition metal tungstates for photoelectrochemical water oxidation: A combined experimental and computational approach

Ana Caravaca, Francisco J. Pastor, Andrés Parra-Puerto*, Nathalia C. Verissimo, Néstor Guijarro, Teresa Lana-Villarreal, and Roberto Gómez*

Institut Universitari d'Electroquímica i Departament de Química Física, Universitat d'Alacant, Apartat 99, E-03080 Alicante, Spain.

*Corresponding authors

Email: roberto.gomez@ua.es, andres.parra@ua.es

Index

Table of Figures

List of Tables

1. Materials

Citric acid monohydrate ($C_6H_8O_7 \cdot H_2O$; 99% from VWR) and cobalt (II) nitrate hexahydrate ($Co(NO_3)_2 \cdot 6H_2O$; 99.99% from VWR); ammonium (meta)tungstate hydrate (AMT) ($H_{43}N_6O_{41}W_{12}$; 99% from Indagoo); manganese (II) nitrate tetrahydrate ($Mn(NO_3)_2 \cdot 4H_2O$; 97% Merk) and copper (II) nitrate trihydrate ($Cu(NO_3)_2 \cdot 3H_2O$; 99.99% Merk); nickel (II) nitrate hexahydrate ($Ni(NO_3)_2 \cdot 6H_2O$; ≥ 98.5% Fluka) and zinc nitrate hexahydrate ($Zn(NO_3)_2 \cdot 6H_2O$; 98% Fluka); iron (II) chloride tetrahydrate ($FeCl_2 \cdot 4H_2O$; 98% Thermo Scientific) and 2-methoxyethanol ($C_3H_8O_2$; 99% Thermo Scientific).

2. Digital pictures of the precursor solutions

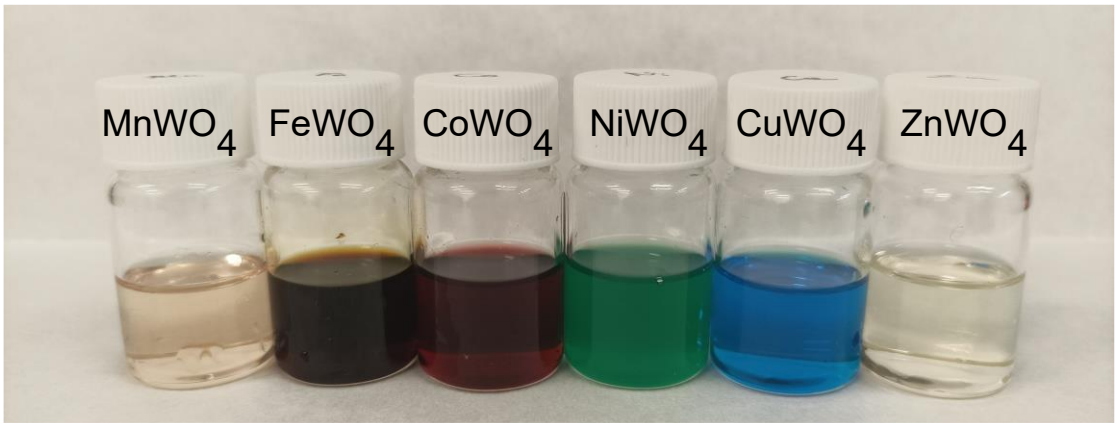

Figure S1. Precursor solutions of the Mn, Fe, Co, Ni, Cu and Zn tungstates.

3. Synthesis reactions

Synthesis reactions **Eq. S1** and **S2**:

$$12\ RCl_2(aq) + (NH_4)_6H_2W_{12}O_{40}(aq) + 8H_2O(l) \rightarrow 12RWO_4(s) + 6NH_3(g) + 24HCl(g) \quad (S1)$$

$$12\ R(NO_3)_2(aq) + (NH_4)_6H_2W_{12}O_{40}(aq) + 40H_2O(l) \rightarrow 12RWO_4(s) + 6NH_3(g) + 24HNO_3 + 32H_2O(g) \quad (S2)$$

4. $CuWO_4$ and $FeWO_4$ Layers

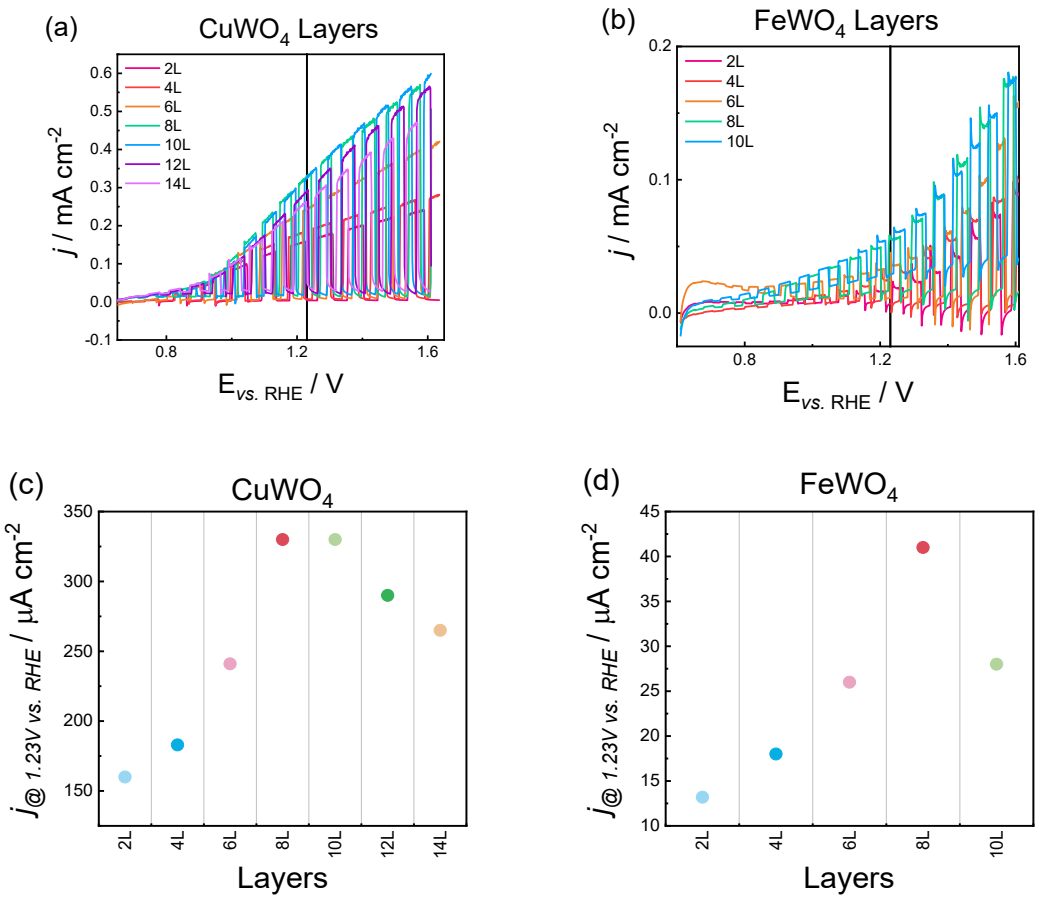

Figure S2. LSVs for $CuWO_4$ (a) and $FeWO_4$ (b) electrodes with different numbers of layers, and a graphical representation of the current density of those samples at 1.23V *vs*. RHE (c and d, respectively).

5. DFT computational details

The structures extracted from the Crystallographic Open Database (COD) were subject to calculations for: a) evaluating the ferro/antiferromagnetic behavior, b) optimizing the geometry, and c) obtaining the DOS profile.

The ferro/antiferromagnetic calculations have been carried out with a k-point density per unit cell of 500, an electronic convergence criterion of $1 \cdot 10^{-4}$ eV. The geometry optimization was done with an electronic convergence criterion of $1 \cdot 10^{-6}$ eV, a geometric convergence criterion of forces below 0.01 eV·Å^{-1} and a k-point density per unit cell of 1500. For obtaining the DOS profiles, a single-point calculation was performed with an electronic convergence criterion of $1 \cdot 10^{-8}$V and a k-point density per unit cell of 15000.

The Boltztrap 2 code was used to get the effective masses of the charge carriers from the PBE+U electronic structure.[1] These effective masses have been estimated from a parabolic band model (Eq. S3).

$$E(k) = E_0 + \frac{\hbar^2 k^2}{2m^*} \quad \text{(S3)}$$

where m* is the effective mass of the electrons/holes in the band, E(k) is the energy of an electronic state with wavevector *k* (describes the electron momentum in the reciprocal space), E_0 is the band-edge energy (minimum energy of the conduction band or maximum energy of the valence band), and ħ is the reduced Planck's constant.

6. U_{eff} values used in PBE+U

Table S1. U_{eff} values used in PBE+U for the different elements that compose the tungstates.

Element	**W**	**Mn**	**Fe**	**Co**	**Ni**	**Cu**	**Zn**
U_{eff} / eV	4.0	3.0	3.0	2.8	5.0	6.7	4.0

7. Theoretical values for the indirect band gaps

Table S2. Indirect Band gap (E^{Ind}_g) obtained from the band structure.

Material	Transition	E^{Ind}_g / eV
$MnWO_4$	D→M	2.38
$FeWO_4$	X→Z	1.44
$CoWO_4$	Γ→Z	2.11
$NiWO_4$	R → Γ	2.95
$CuWO_4$	Γ →L	2.04
$ZnWO_4$	Γ-Z→ Y	2.76

8. SEM

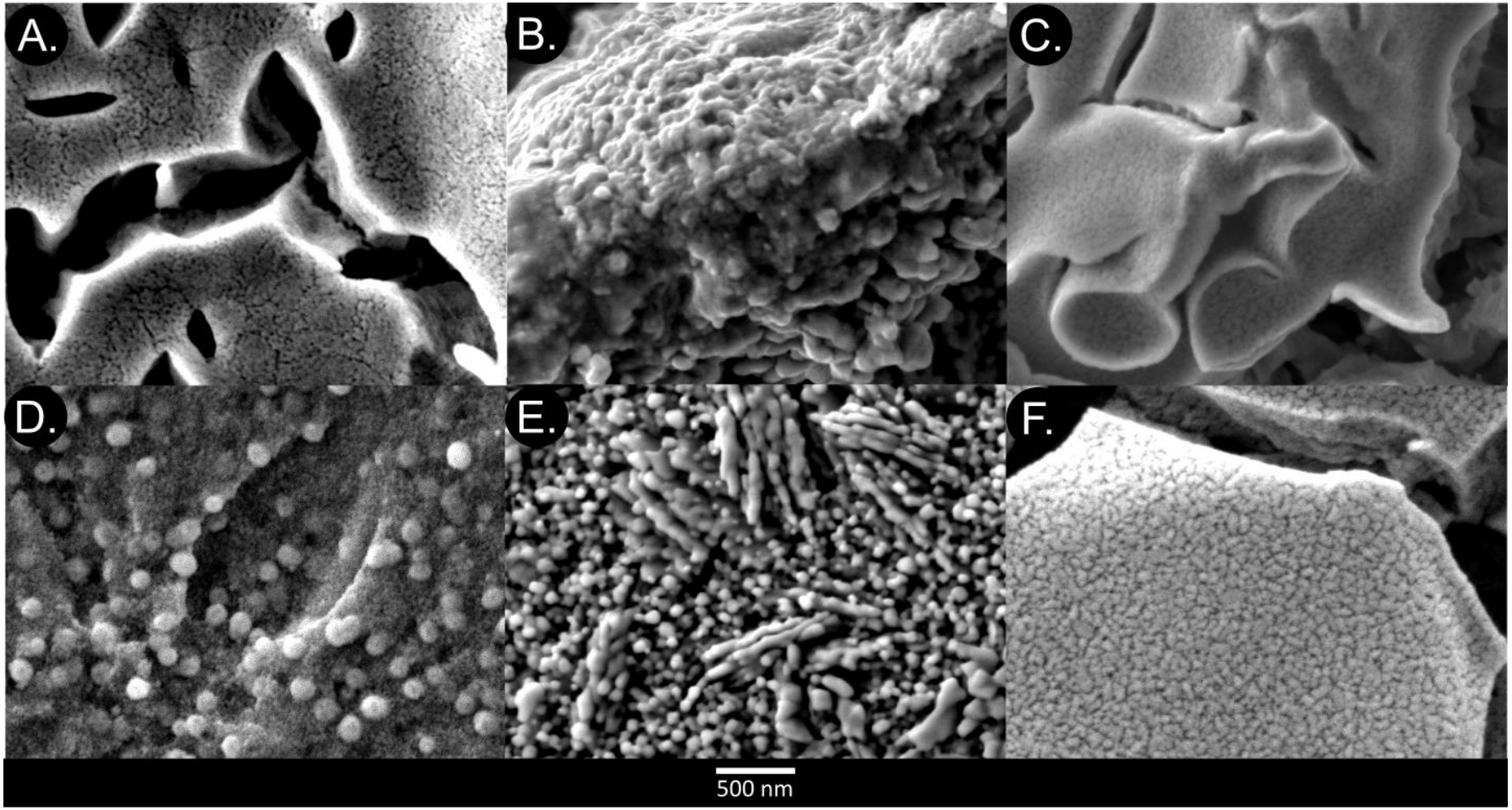

Figure S3. SEM top-view of (a) Mn, (b) Fe, (c) Co, (d) Ni, (e) Cu and (f) Zn tungstate films.

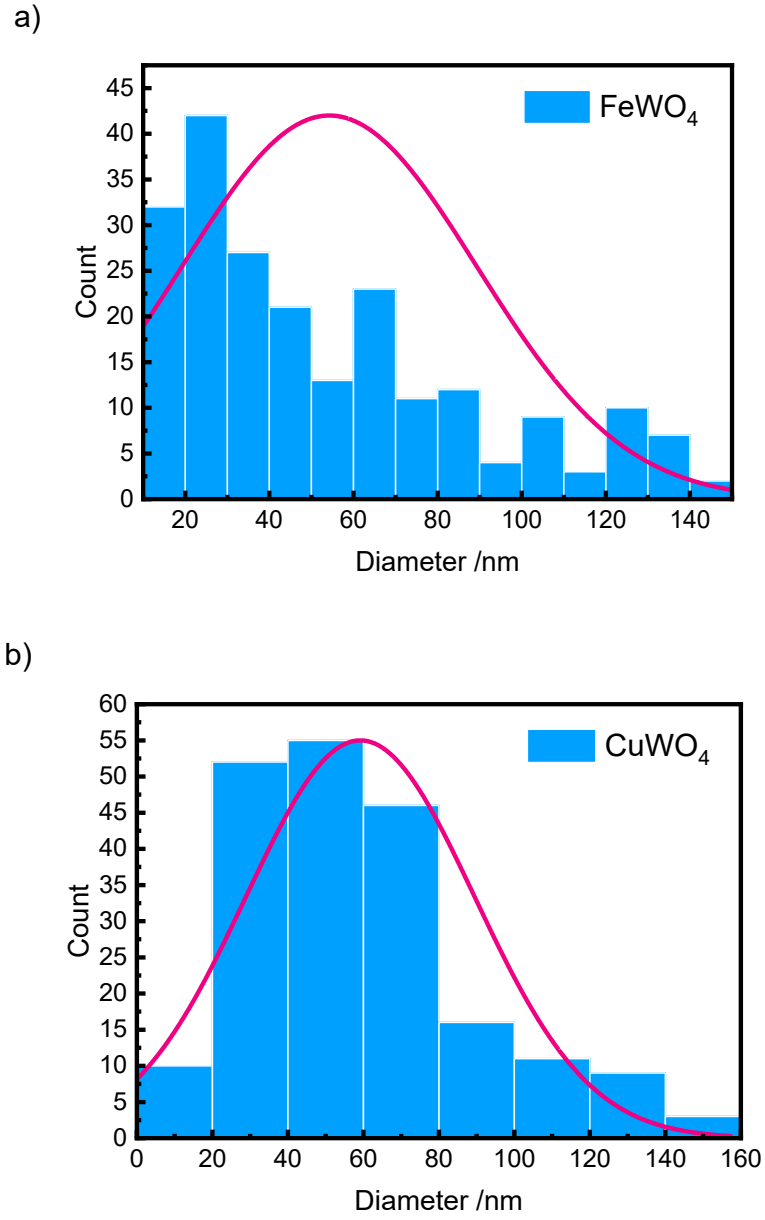

Figure S4. Particle size histograms for (a) Cu and (b) Fe tungstate films.

9. EDS

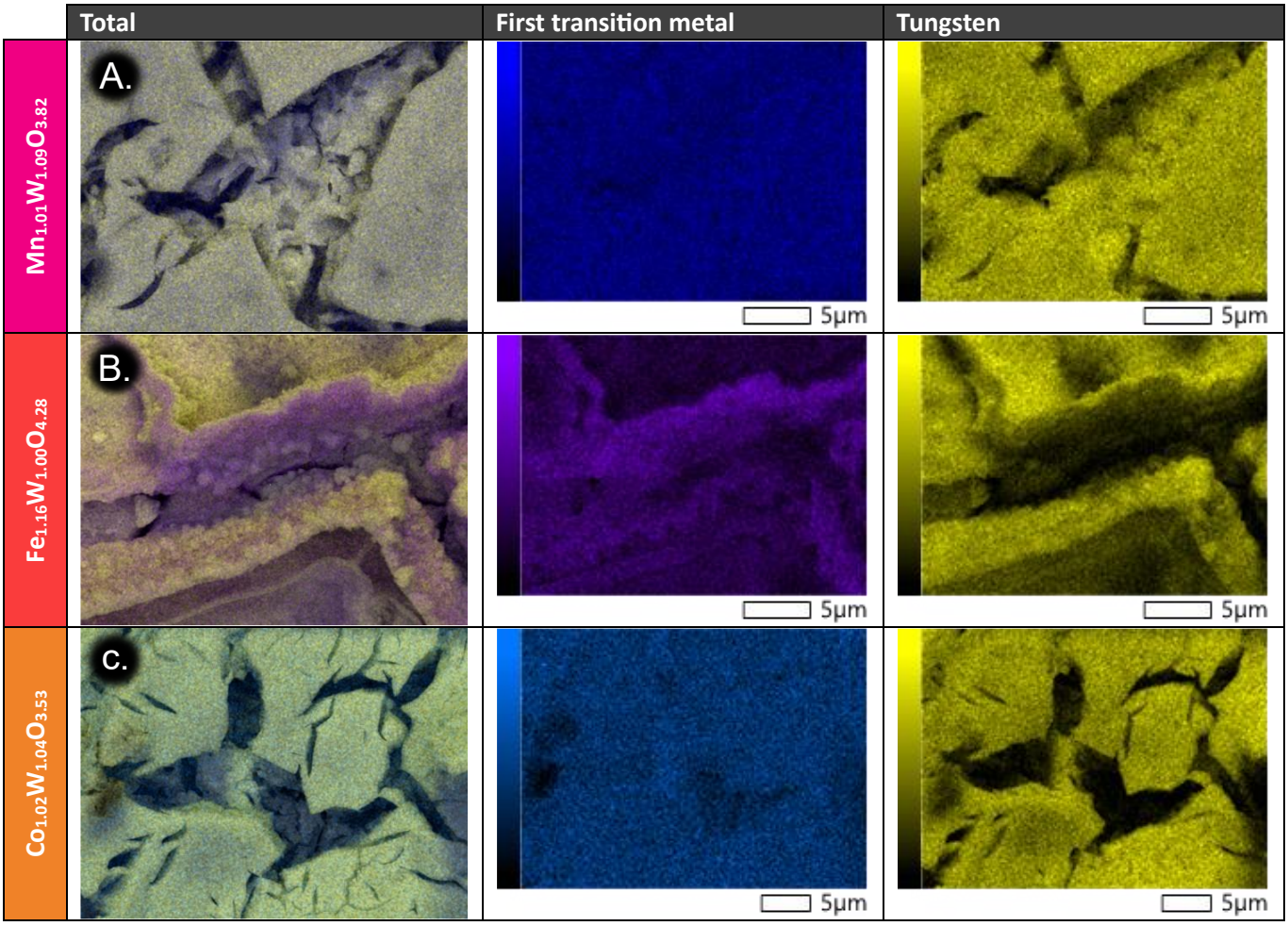
Total
First transition metal
Tungsten
$Mn_{1.01}W_{1.09}O_{3.82}$
$Fe_{1.16}W_{1.00}O_{4.28}$
$Co_{1.02}W_{1.04}O_{3.53}$
A.
B.
C.
5µm
5µm
5µm
5µm
5µm
5µm

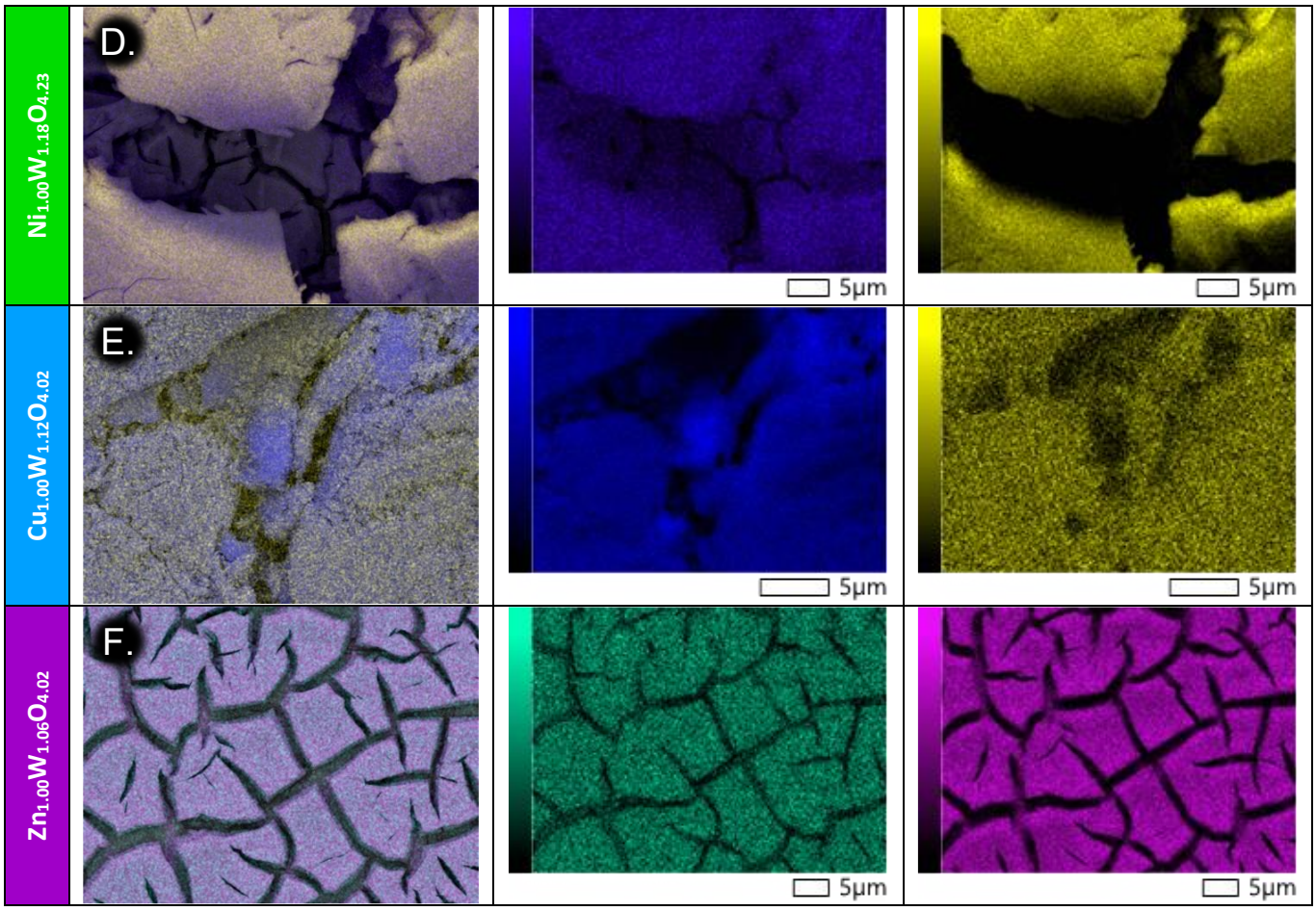

Figure S5. EDS pictures of all the analyzed elements together, R-element and tungsten (from left to right) for all the RWO_4 (from Mn to Zn).

10. XRD

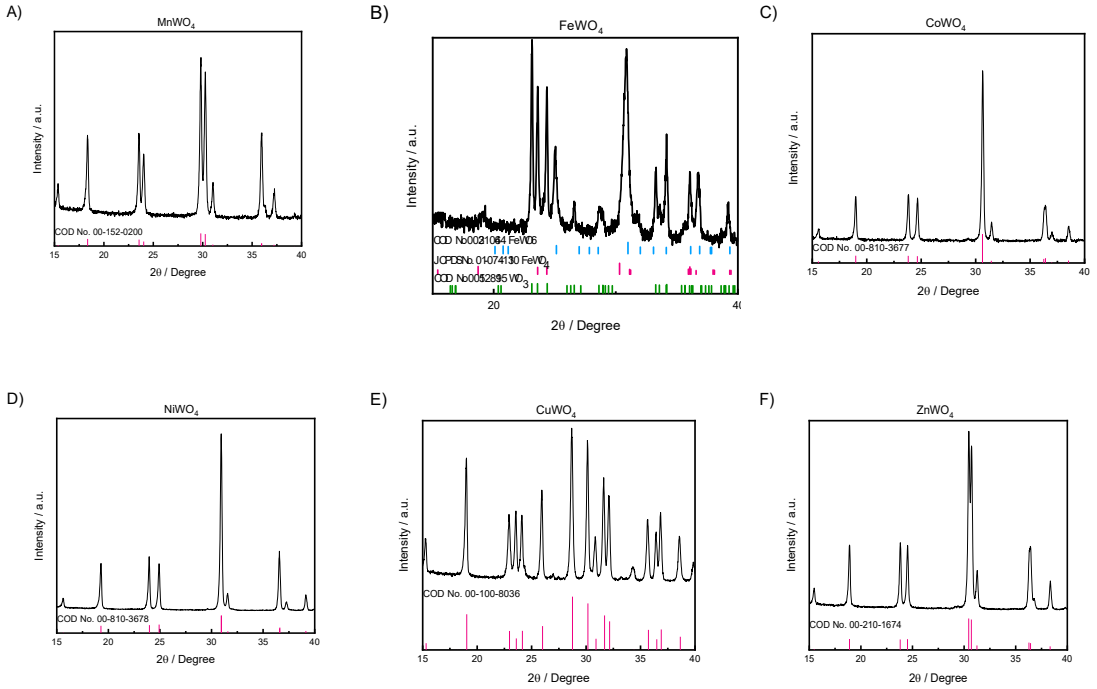

Figure S6. XRD for the RWO_4 tungstates (powder) and their identification cards. A) $MnWO_4$, B) $FeWO_4$, C) $CoWO_4$, D) $NiWO_4$, E) $CuWO_4$ and F) $ZnWO_4$.

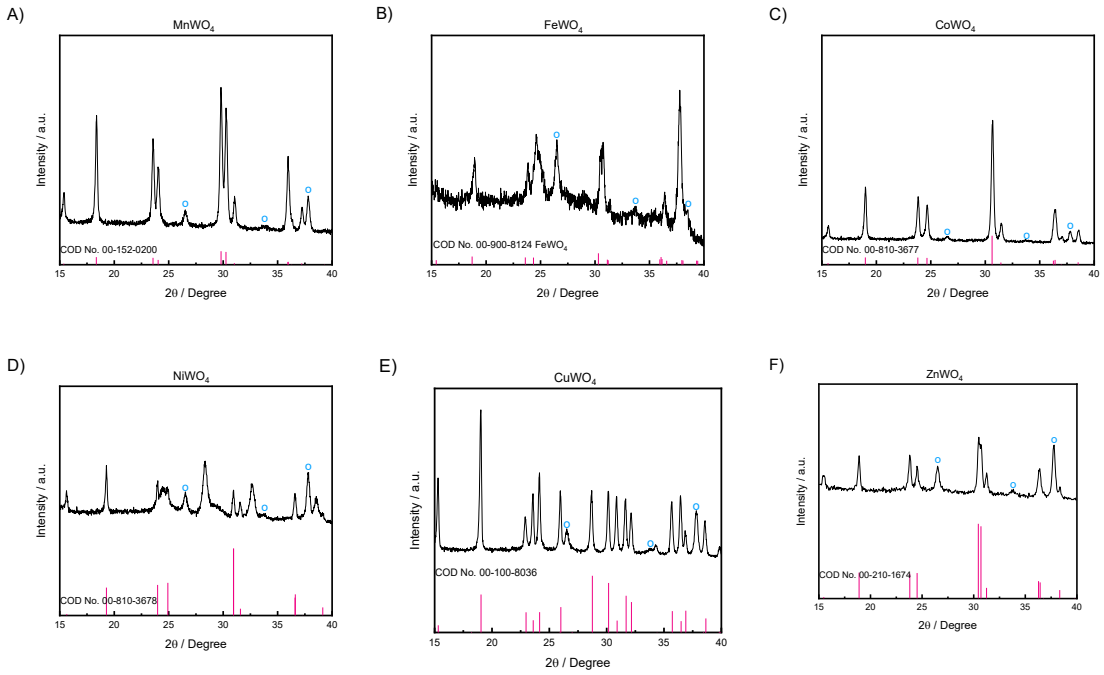

Figure S7. XRD for the RWO_4 tungstates (thin films) and their identification cards. A) $MnWO_4$, B) $FeWO_4$, C) $CoWO_4$, D) $NiWO_4$, E) $CuWO_4$ and F) $ZnWO_4$. FTO peaks labeled with blue open circles.

The diffractograms in Figure S6. XRD for the RWO_4 tungstates (powder) and their identification cards. A) $MnWO_4$, B) $FeWO_4$, C) $CoWO_4$, D) $NiWO_4$, E) $CuWO_4$ and F) $ZnWO_4$. and S7 are similar for most of the samples, except for $FeWO_4$ and $NiWO_4$. In the $FeWO_4$ case and in contrast with the corresponding powders, neither WO_3 nor Fe(III)-related impurities were detected in the thin film. This could result from the role of FTO as a heterogeneous nucleation surface, which could favor the growth of $FeWO_4$ over that of the impurities.

The Scherrer equation (Eq S4) was employed to obtain an average crystal size for the different samples.

$$D = \frac{K\lambda}{\beta cos\theta} \quad \text{(S4)}$$

where D is the crystal size (nm), K is the Scherrer constant (0.9), λ is the wavelength of the X-ray source (0.15406 nm), β is the full width at half maximum (FWMH), and θ is the Bragg angle of the peak.

The most significant peaks in the diffractograms were used to obtain the crystal size (**Table S3**), which is similar for all the samples, except for $ZnWO_4$. It seems thus that the crystal size of the samples is not key for explaining the observed differences in the photoelectrochemical responses.

Table S3. Summary of the crystal size in the tungstate thin films from the full width at half maximum of the main XRD peaks.

Sample	2θ / degrees	FWHM / degrees	Crystallite size /nm
$MnWO_4$	30	0.34	27
$FeWO_4$	38	0.40	23
$CoWO_4$	31	0.40	23
$NiWO_4$	20	0.42	22
$CuWO_4$	19	0.40	23
$ZnWO_4$	31	1.00	9

11. Tests to discard the presence of significant amounts of WO_3 on $FeWO_4$

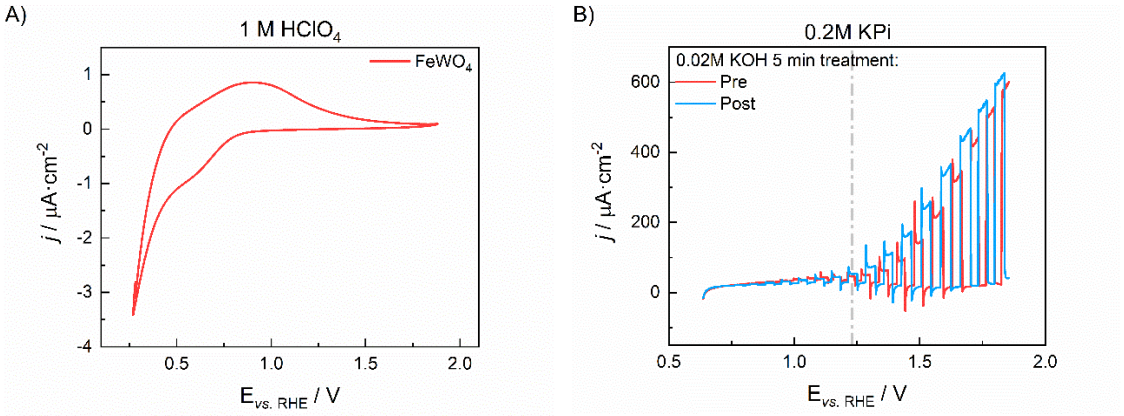

Figure S8. (a) CVs in the dark for N_2-purged 1 M $HClO_4$. (b) LSV in 0.2 M KPi for $FeWO_4$ samples before and after being immersed for 5 min in a 0.02 M KOH solution.

The $FeWO_4$ dark CV (**Figure S8a**) is rather different from that of WO_3 under the same conditions.[2] More significantly, **Figure S8**. (a) CVs in the dark for N_2-purged 1 M $HClO_4$. (b) LSV in 0.2 M KPi for $FeWO_4$ samples before and after being immersed for 5 min in a 0.02 M KOH solution.

b shows LSVs for $FeWO_4$ before and after being treated for 5 min in a 0.02 M KOH solution. The photocurrents at 1.23 V *vs*. RHE (and in the whole potential range) are similar in both cases. As any surface WO_3 would be dissolved in the alkaline solution, this result supports the fact that WO_3 is absent from the surface of as-prepared $FeWO_4$ thin films.

12. Band gaps

Table S4. Direct and indirect band gaps, E_g^{Dir} and E_g^{In} obtained experimentally and theoretically (PBE+U) as well as values reported in the literature (E_g^{Bib}).

Sample	$E_g^{Dir-Exp}$ / eV	E_g^{In-Exp} / eV	$E_g^{Bib-Exp}$ / eV		$E_g^{Exp-DFT}$ / eV	$E_g^{Bib-DFT}$ / eV
			Direct	Indirect		
$MnWO_4$	2.90	2.84	2.70-2.88[3–5]	2.63[6]	2.38	2.40[7]
$FeWO_4$	1.96	1.89	1.70-2.16[4,8,9]	1.95[10]	1.44	2.00[11]
$CoWO_4$	2.90	2.78	2.70-2.86[12–14]	2.25[15]	2.11	2.33[15]
$NiWO_4$	3.22	3.13	2.80-3.67[16–18]	2.25[19]	2.95	2.7[20]
$CuWO_4$	2.57	2.37	2.32-2.74[21,22]	2.37[23,24]	2.04	2.27[20]
$ZnWO_4$	3.81	3.73	3.88[25]	2.67[26]	2.76	3.77[27]

13. Flat bands potentials

Table S5. E_{fb} as obtained by determining onset potentials with chopped illumination in 0.2M KPi and values reported in the literature.

	Flat band / V_{RHE}	Reported
$MnWO_4$	0.88 V	0.98[28]

$FeWO_4$	0.50 V	0.73[29]
$CoWO_4$	0.58 V	0.47[30]
$NiWO_4$	0.55 V	0.48[31]
$CuWO_4$	0.60 V (0.5 in MS, 0.65 in OCP)	0.65[32]
$ZnWO_4$	0.55	0.20[33]

Different methods were followed to obtain the flat band potentials of RWO_4. These approaches were:

i. Mott-Schottky

Mott-Schottky (MS) plots were obtained by performing Electrochemical Impedance Spectroscopy measurements at frequencies ranging from 10^5 Hz to 0.1 Hz with an amplitude of 10 mV and at applied potentials from 0.74 to 1.64 V_{RHE}. Bode and Nyquist plots were recorded for each potential and RWO_4.

This method allows for the determination of the flat band potential by measuring the differential capacitance of the semiconductor-electrolyte interface. The Mott-Schottky equation (**Eq. S5**) for an n-type material is:

$$\frac{1}{C_{sc}^2} = \frac{2}{\varepsilon_0 \varepsilon_r e n}\left(E - E_{fb} - \frac{k_b T}{e}\right) \quad \text{(S5)}$$

Where C_{sc} is the capacitance, ε_0 is the vacuum permittivity, ε_r the dielectric constant of the semiconductor, e the elementary charge, n the density of donors, E the applied electrode potential, E_{fb} the flat band potential, k_b the Boltzmann constant and T the temperature.

The equivalent circuit used for obtaining the Mott-Schottky capacitance values is depicted in **Scheme S1**.

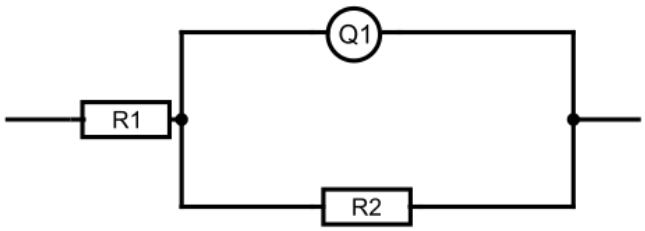

Scheme S1. Equivalent circuit for $CuWO_4$. Being R the elements for resistance, and Q the CPE (constant phase element).

This circuit was applied to each Nyquist plot with the Z-view software. Resistance and CPE parameters were obtained. To estimate C_{sc} from the CPE, eqs. S6-8 were applied:

$$C_{SC} = Q \cdot (\omega_{max})^{n-1} \quad \text{(S6)}$$

$$\omega_{max} = (\frac{1}{R_2 \cdot Q})^{1/n} \quad \text{(S7)}$$

$$C_{SC} = Q^{1/n} \cdot R_2^{\frac{1-n}{n}} \quad \text{(S8)}$$

where Q is the CPE constant, n the CPE exponent, ω the frequency, and R the resistance.

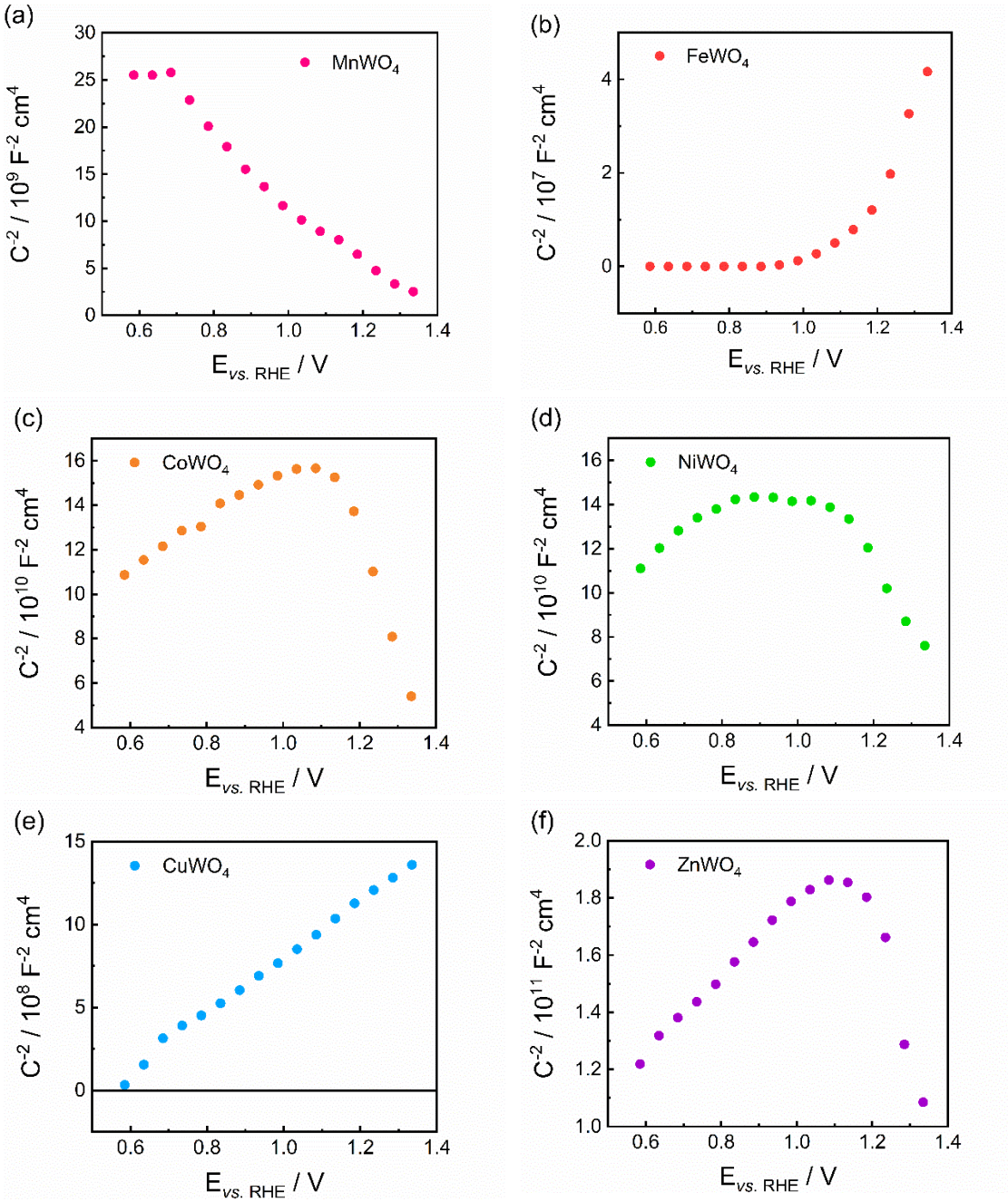

Figure S9. Mott-Schottky (MS) plots for RWO_4 electrodes (R = Mn, Fe, Co, Ni, Cu and Zn) in 0.1 M KPi.

To estimate the $CuWO_4$ donor density, Eq. S9 was used.

$$n_D = \frac{2}{\varepsilon_0 \varepsilon_r e m} \quad \text{(S9)}$$

Here, n_D is the donor density (m^{-3}), ε_0 is the vacuum permittivity ($8.85 \cdot 10^{-12}$ F m^{-1}), ε_r is the dielectric constant of the material (83 for $CuWO_4$), e is the elementary charge ($1.60 \cdot 10^{-19}$ C), and m is the slope of the MS plot (F^{-2} m^4) . In our case, $CuWO_4$ has a donor density (n_D) of $9.7 \cdot 10^{20}$ cm^{-3}.

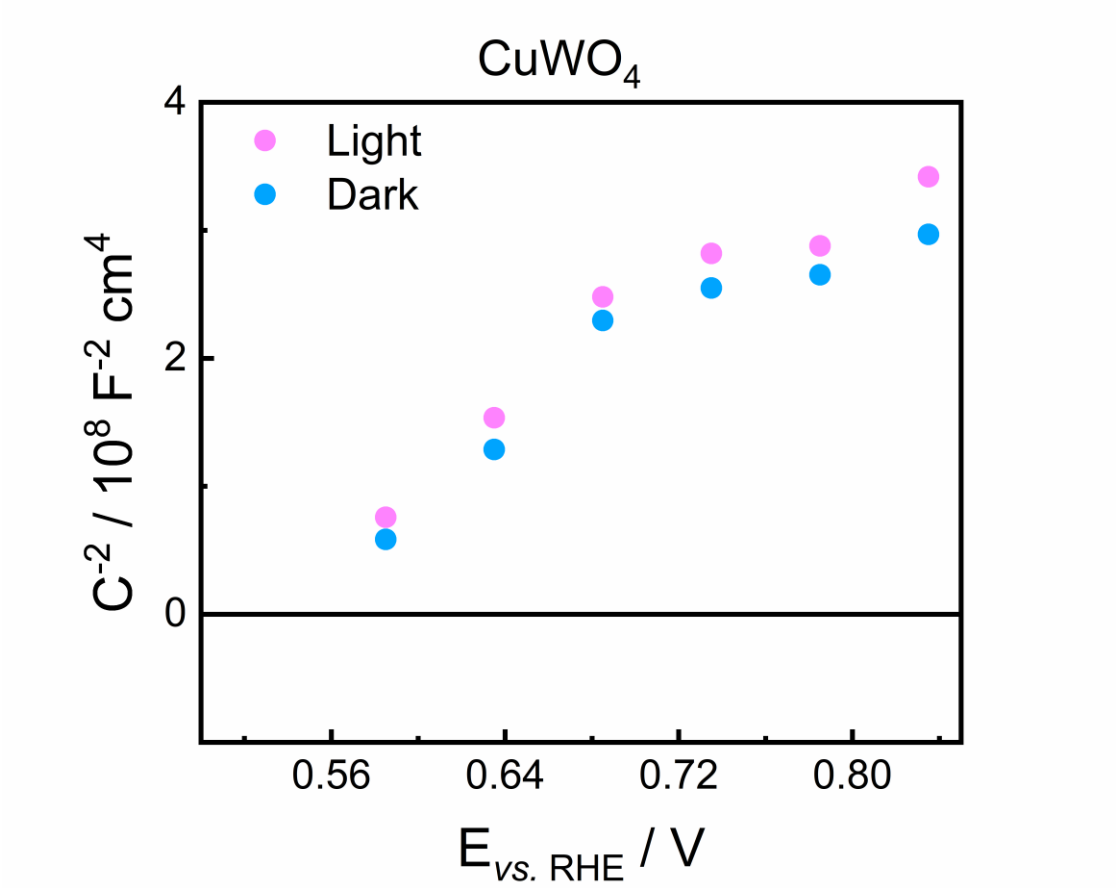

Figure S10. MS plot for a $CuWO_4$ electrode both under illumination (100 mW cm^{-2}) and in the dark.

As can be seen in Figure S10, $CuWO_4$ follows the BEP regime both under illumination and in the dark. Importantly, the MS plots are almost identical in both cases, which indicated that illumination does not cause band unpinning.

Table S6. Mott-Schottky data obtained by Nyquist plots fitting with Z-view software.

	$MnWO_4$														
E / V	-0.05	0	0.05	0.1	0.15	0.2	0.25	0.3	0.35	0.4	0.45	0.5	0.55	0.6	0.65
R_2/Ω	$2.7\cdot10^{04}$	$2.7\cdot10^{04}$	$3.0\cdot10^{04}$	$3.1\cdot10^{04}$	$3.0\cdot10^{04}$	$3.0\cdot10^{04}$	$2.9\cdot10^{04}$	$2.8\cdot10^{04}$	$2.8\cdot10^{04}$	$2.6\cdot10^{04}$	$2.3\cdot10^{04}$	$2.1\cdot10^{04}$	$2.0\cdot10^{04}$	$2.0\cdot10^{04}$	$2.0\cdot10^{04}$
$Q/\Omega^{-1}s^n$	$7.5\cdot10^{-06}$	$7.5\cdot10^{-06}$	$7.4\cdot10^{-06}$	$7.8\cdot10^{-06}$	$8.3\cdot10^{-06}$	$8.8\cdot10^{-06}$	$9.4\cdot10^{-06}$	$1.0\cdot10^{-05}$	$1.1\cdot10^{-05}$	$1.2\cdot10^{-05}$	$1.3\cdot10^{-05}$	$1.4\cdot10^{-05}$	$1.5\cdot10^{-05}$	$1.8\cdot10^{-05}$	$2.1\cdot10^{-05}$
n	0.90	0.90	0.90	0.90	0.89	0.89	0.89	0.89	0.88	0.87	0.86	0.85	0.84	0.83	0.82
	$FeWO_4$														
R_2/Ω	$1.0\cdot10^{+20}$	$1.0\cdot10^{+20}$	$1.0\cdot10^{+20}$	$6.9\cdot10^{+20}$	$1.1\cdot10^{+18}$	$5.5\cdot10^{+11}$	$5.4\cdot10^{+11}$	$2.8\cdot10^{+06}$	$8.3\cdot10^{+05}$	$5.0\cdot10^{+05}$	$4.0\cdot10^{+05}$	$3.7\cdot10^{+05}$	$3.4\cdot10^{+05}$	$3.0\cdot10^{+05}$	$2.6\cdot10^{+05}$
$Q/\Omega^{-1}s^n$	$1.3\cdot10^{-03}$	$9.3\cdot10^{-04}$	$6.5\cdot10^{-04}$	$5.2\cdot10^{-04}$	$3.6\cdot10^{-04}$	$2.8\cdot10^{-04}$	$2.3\cdot10^{-04}$	$1.9\cdot10^{-04}$	$1.6\cdot10^{-04}$	$1.4\cdot10^{-04}$	$1.2\cdot10^{-04}$	$9.9\cdot10^{-05}$	$8.5\cdot10^{-05}$	$7.4\cdot10^{-05}$	$6.4\cdot10^{-05}$
n	0.82	0.83	0.81	0.81	0.76	0.75	0.74	0.74	0.74	0.74	0.74	0.74	0.73	0.74	0.74
	$CoWO_4$														
R_2/Ω	$5.2\cdot10^{+04}$	$4.1\cdot10^{+04}$	$2.6\cdot10^{+04}$	$5.5\cdot10^{+04}$	$6.0\cdot10^{+04}$	$5.7\cdot10^{+04}$	$5.9\cdot10^{+04}$	$5.9\cdot10^{+04}$	$5.9\cdot10^{+04}$	$5.9\cdot10^{+04}$	$5.9\cdot10^{+04}$	$5.8\cdot10^{+04}$	$5.8\cdot10^{+04}$	$5.8\cdot10^{+04}$	$5.7\cdot10^{+04}$
$Q/\Omega^{-1}s^n$	$3.3\cdot10^{-06}$	$3.4\cdot10^{-06}$	$3.7\cdot10^{-06}$	$3.2\cdot10^{-06}$	$3.1\cdot10^{-06}$	$3.0\cdot10^{-06}$	$3.0\cdot10^{-06}$	$2.9\cdot10^{-06}$	$2.9\cdot10^{-06}$	$2.9\cdot10^{-06}$	$2.9\cdot10^{-06}$	$2.9\cdot10^{-06}$	$3.1\cdot10^{-06}$	$3.5\cdot10^{-06}$	$4.1\cdot10^{-06}$
n	0.93	0.93	0.92	0.93	0.93	0.93	0.93	0.93	0.93	0.93	0.93	0.93	0.92	0.92	0.91
	$NiWO_4$														
R_2/Ω	$3.1\cdot10^{+04}$	$3.4\cdot10^{+04}$	$3.8\cdot10^{+04}$	$3.9\cdot10^{+04}$	$4.0\cdot10^{+04}$	$4.0\cdot10^{+04}$	$4.1\cdot10^{+04}$	$4.2\cdot10^{+04}$	$4.2\cdot10^{+04}$	$4.1\cdot10^{+04}$	$4.1\cdot10^{+04}$	$4.2\cdot10^{+04}$	$4.2\cdot10^{+04}$	$4.2\cdot10^{+04}$	$4.3\cdot10^{+04}$
$Q/\Omega^{-1}s^n$	$3.7\cdot10^{-06}$	$3.5\cdot10^{-06}$	$3.4\cdot10^{-06}$	$3.3\cdot10^{-06}$	$3.3\cdot10^{-06}$	$3.2\cdot10^{-06}$	$3.2\cdot10^{-06}$	$3.2\cdot10^{-06}$	$3.3\cdot10^{-06}$	$3.3\cdot10^{-06}$	$3.3\cdot10^{-06}$	$3.4\cdot10^{-06}$	$3.6\cdot10^{-06}$	$4.0\cdot10^{-06}$	$4.3\cdot10^{-06}$
n	0.91	0.91	0.91	0.91	0.91	0.91	0.91	0.91	0.90	0.90	0.90	0.90	0.89	0.88	0.88
	$CuWO_4$														
R_2/Ω	$5.0\cdot10^{+03}$	$8.9\cdot10^{+03}$	$1.9\cdot10^{+04}$	$3.3\cdot10^{+04}$	$4.2\cdot10^{+04}$	$4.7\cdot10^{+04}$	$5.1\cdot10^{+04}$	$5.3\cdot10^{+04}$	$5.5\cdot10^{+04}$	$5.6\cdot10^{+04}$	$5.6\cdot10^{+04}$	$5.7\cdot10^{+04}$	$5.8\cdot10^{+04}$	$6.0\cdot10^{+04}$	$6.2\cdot10^{+04}$
$Q/\Omega^{-1}s^n$	$1.8\cdot10^{-04}$	$8.5\cdot10^{-05}$	$5.6\cdot10^{-05}$	$4.8\cdot10^{-05}$	$4.4\cdot10^{-05}$	$4.0\cdot10^{-05}$	$3.7\cdot10^{-05}$	$3.5\cdot10^{-05}$	$3.3\cdot10^{-05}$	$3.1\cdot10^{-05}$	$3.0\cdot10^{-05}$	$2.8\cdot10^{-05}$	$2.7\cdot10^{-05}$	$2.6\cdot10^{-05}$	$2.6\cdot10^{-05}$
n	0.76	0.84	0.89	0.89	0.89	0.88	0.87	0.87	0.86	0.85	0.85	0.84	0.84	0.84	0.83
	$ZnWO_4$														

R_2/Ω	$1.6\cdot10^{+04}$	$3.7\cdot10^{+04}$	$8.1\cdot10^{+04}$	$1.2\cdot10^{+05}$	$1.3\cdot10^{+05}$	$1.3\cdot10^{+05}$	$1.4\cdot10^{+05}$	$1.3\cdot10^{+05}$	$1.3\cdot10^{+05}$	$1.4\cdot10^{+05}$	$1.4\cdot10^{+05}$	$1.3\cdot10^{+05}$	$1.3\cdot10^{+05}$	$1.3\cdot10^{+05}$	$1.3\cdot10^{+05}$
$Q/\Omega^{-1}s^n$	$3.5\cdot10^{-06}$	$3.2\cdot10^{-06}$	$2.9\cdot10^{-06}$	$2.8\cdot10^{-06}$	$2.7\cdot10^{-06}$	$2.7\cdot10^{-06}$	$2.6\cdot10^{-06}$	$2.6\cdot10^{-06}$	$2.5\cdot10^{-06}$	$2.5\cdot10^{-06}$	$2.5\cdot10^{-06}$	$2.5\cdot10^{-06}$	$2.5\cdot10^{-06}$	$2.7\cdot10^{-06}$	$3.0\cdot10^{-06}$
n	0.93	0.94	0.94	0.95	0.95	0.95	0.95	0.95	0.95	0.94	0.94	0.94	0.94	0.93	0.92

ii. Open Circuit Potential (OCP)

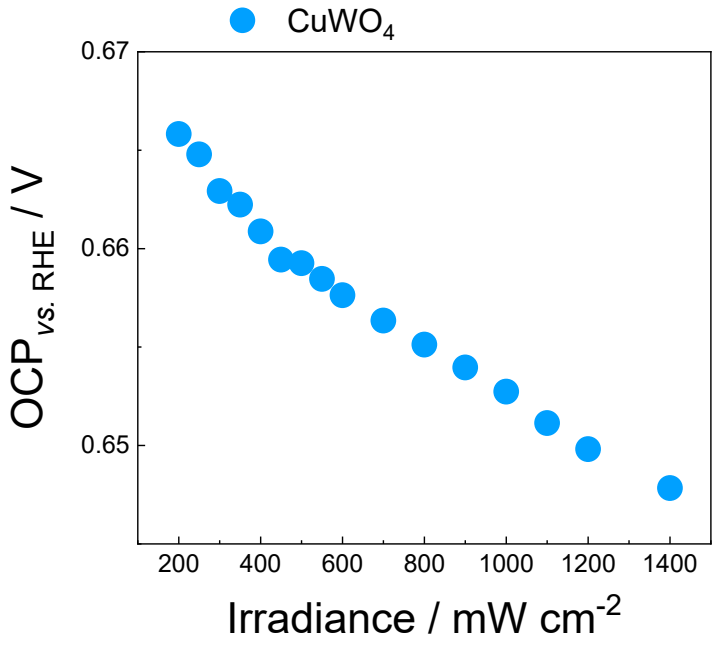

Figure S11. Steady-state OCP at different light intensities for $CuWO_4$.

OCP measurements were performed until obtaining a steady-state value at different light intensities (from 200 to 1400 mW cm^{-2}). In principle, the steady state OCP under intense illumination value approximately corresponds to the flat band potential, which in this case has a value of around 0.64 V_{RHE}.

iii. Current-potential scans under chopped illumination

This method is based on determining the potential at which (for n-type semiconductors) a stable photoanodic response starts, which is approximately equal to the flat band potential. It signals the potential at which the band bending starts (if band edge pinning prevails).[34] The measurements were conducted at a slow positive going scan rate (1 mV s^{-1}) under periodically interrupted illumination in 0.1 M Na_2SO_4.

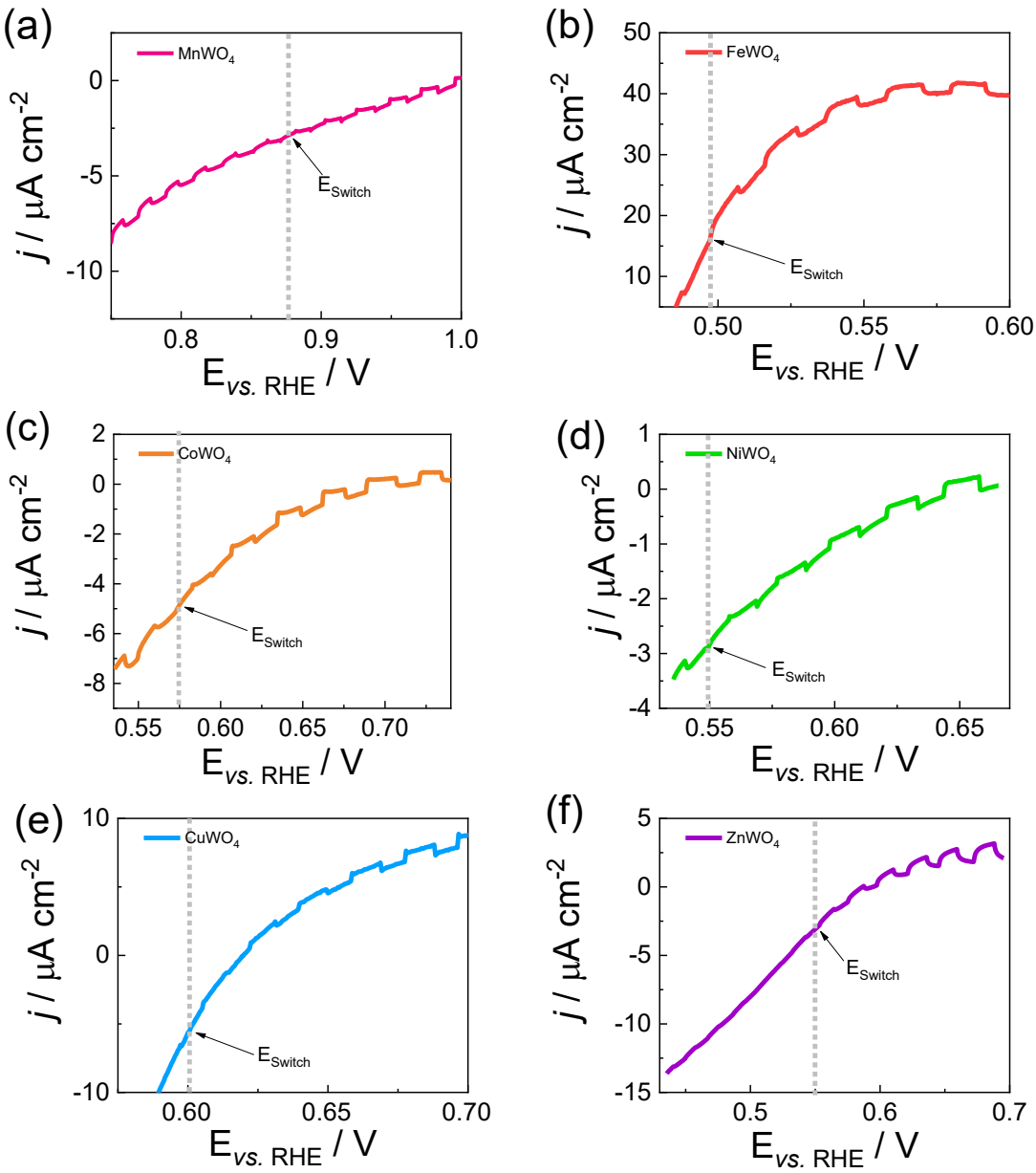

Figure S12. LSV for RWO_4 electrodes in 0.1 M Na_2SO_4 under 1 W cm^{-2} chopped illumination for the complete tungstate series: a) Mn, b) Fe, c) Ni, d) Cu and f) Zn. The grey dotted lines indicate the E_{fb} value

14. Thickness and Photoresponse

By adjusting the preparation conditions (number of layers), films of comparable thickness were prepared for the different tungstates (**Table S7**).

Table S7. Film thickness of RWO_4 samples

Sample	Film thickness / µm
$MnWO_4$	1.3
$FeWO_4$	1.4
$CoWO_4$	1.3
$NiWO_4$	1.5
$CuWO_4$	1.2
$ZnWO_4$	1.6

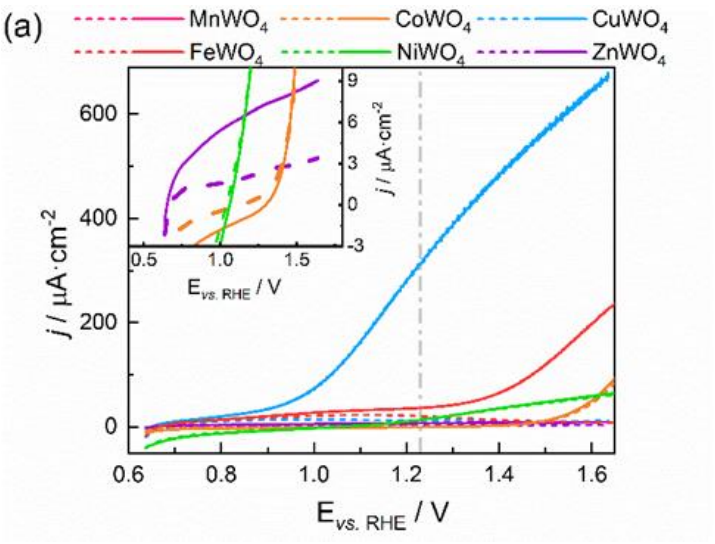

Figure S13. LSVs for RWO_4 electrodes with the thickness of **Error! Reference source not found.**7 in phosphate buffer solution (pH 7) both in the dark (dashed lines) and under 100 mW cm^{-2} SE illumination (solid lines) (Ni, Zn, and Co curves are given in the inset). $CuWO_4$ has the same photocurrent as in Figure 7a because the thickness is the optimal.

Both **Figure S13.** LSVs for RWO_4 electrodes with the thickness of Error! Reference source not found.7 in phosphate buffer solution (pH 7) both in the dark (dashed lines) and under 100 mW cm^{-2} SE illumination (solid lines) (Ni, Zn, and Co curves are given in the inset). $CuWO_4$ has the same photocurrent as in Figure 7a because the thickness is the optimal.

and **7** show the same trends, with photocurrents that do not significatively change with moderate variations of the film thickness.

15. Theoretical band edge energies

To obtain the theoretical band edge energies represented in **Figure 4,** it was necessary to first calculate the Fermi level by the method proposed by Butler and Ginley[35] according to Eq. S10:

$$E_F = (\chi_R \chi_W \chi_O^4)^{\frac{1}{7}} \quad \text{(S10)}$$

where χ is the electronegativity of the corresponding element in the Mulliken scale. Then, half of the theoretical band gap (of the corresponding RWO_4) obtained by DFT calculations is either added or subtracted to the Fermi level. This method is only approximate. Deviations from experimental results are not unexpected.

16. Comparison with literature

Table S8. Comparison of RWO_4 electrode related information in this work and in the bibliography, the **irradiation power** in all cases is **100 mW cm^{-2}**.

Photoanode	Synthesis Method	Thermal treatment	Electrolyte	Photocurrent density @1.23V_{RHE} / µA cm^{-2}	Reference
FTO|$MnWO_4$ **FTO|$FeWO_4$** **FTO|$CoWO_4$** **FTO|$NiWO_4$** **FTO|$CuWO_4$** **FTO|$ZnWO_4$**	Sol-gel	550°C for 2h at 3°C/min	0.1 M KPi	- 41 0.0003 0.0007 315 0.0046	**This work**
FTO|$CuWO_4$	Sol-gel	550°C for 2h		20	[32]
FTO|$FeWO_4$ **FTO|$CoWO_4$** **FTO|$NiWO_4$** **FTO|$CuWO_4$**	Polymeric precursors	500°C for 2h at 3°C/min	0.1 M Na_2SO_4	5 21 12.5 30	[36]
FTO|$CuWO_4$ **FTO|$NiWO_4$**	Hydrothermal	550°C for 2h at 3°C/min	0.1 M KPi	230 90	[31]
FTO|$FeWO_4$	Flame synthesis	500°C for 2h	1 M KOH	25	[29]
FTO|$MnWO_4$ **FTO|$CuWO_4$**	Co-precipitation	500 °C for 30 min at 2 °C/min	0.1 M Na_2SO_4	- 19	[37]
FTO|$CoWO_4$	Co-precipitation	500°C for 3h		0.5	[13]
FTO|$CuWO_4$	Hydrothermal	500°C for 2h at 3°C/min	0.2 M KPi	380	[23]
FTO|$CuWO_4$	Sol-gel	500°C for 2h		380	[38]
FTO|$CuWO_4$	Hydrothermal	500°C for 2h		200	[39]
FTO|$CuWO_4$	Sol-gel	550ºC for 2h	0.1 M KPi	480	[40]

17. LSV at different light irradiances

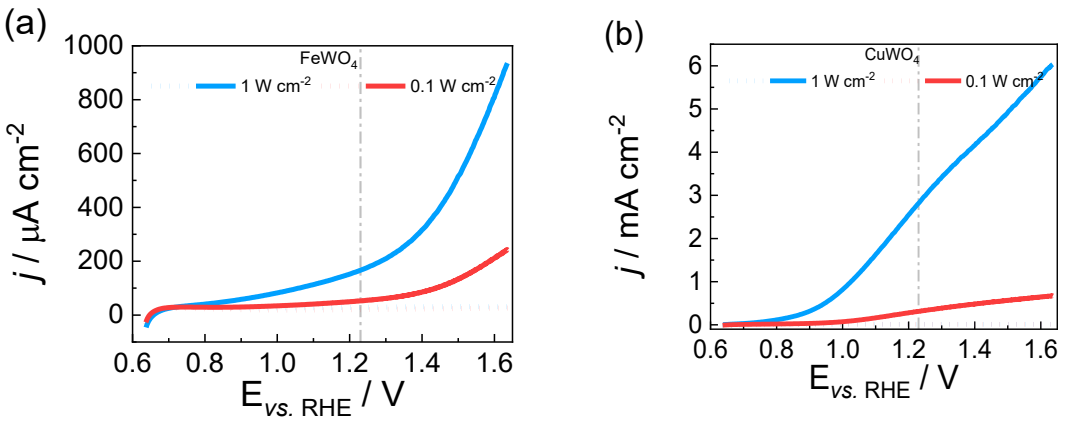

Figure S14. (a), (b) LSVs at 0.1 and 1 W cm^{-2} for $FeWO_4$ and $CuWO_4$ electrodes, respectively. Broken curves were recorded in the dark.

18. Electrolyte-Electrode (EE) illumination

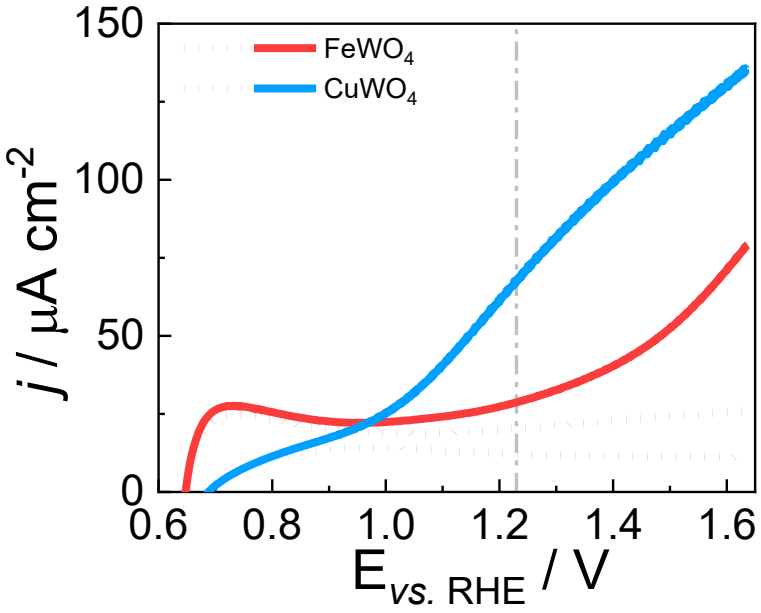

Figure S15. LSV in 0.1 M Na_2SO_4 by EE illumination of the electrodes under 100 mW cm^{-2}, for Fe and Cu tungstates. Continuous lines under irradiation and broken ones in the dark.

19. $CuWO_4$ electron lifetime estimate

To obtain the electron lifetime for $CuWO_4$ (τ), OCP relaxation and CV experiments were carried out in N_2-purged 0.2 M KPi. Electron density at each potential value (n_{ph}) and τ were calculated according to Eqs. S11 and S12, respectively.[41,42]

$$n_{ph} = \frac{1}{eAd}\int_{E_{OC}^{dark}}^{E_{OC}^{(t)}} \frac{I}{v} dE \quad \text{(S11)}$$

$$\tau^{-1} = -\frac{1}{n_{ph}}\frac{dn_{ph}}{dt} \quad \text{(S12)}$$

where e is the elementary charge (1.602×10^{-19} C), A is the electrode area (cm^2), d is the thickness of the electrode (cm), I is the current of the CV (A), v is the scan rate of the CV ($V\ s^{-1}$), and t is the time (s).

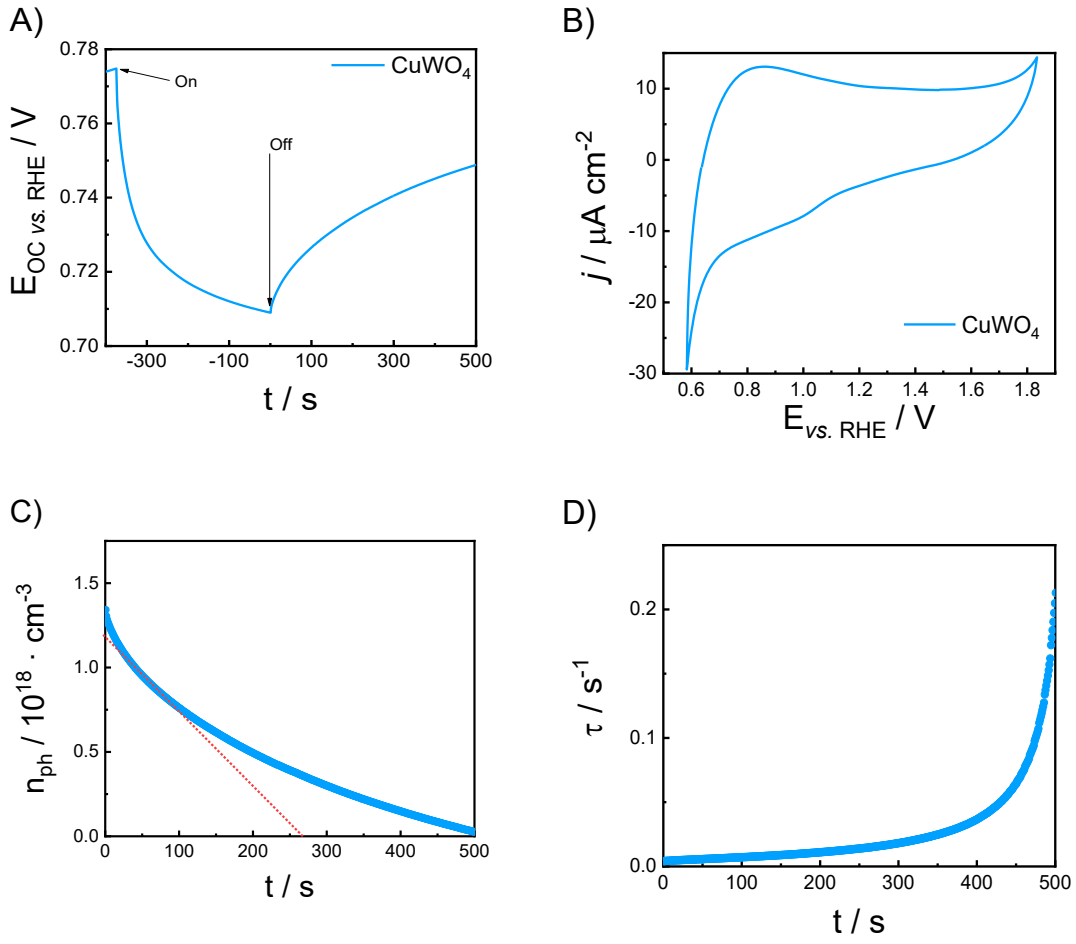

Figure S16. (a) OCP with light chopped on (-350 s) and off (0 s), (b) CV in the dark at 20 mV s^{-1}, (c) electron density (n_{ph}) *vs*. time, (d) electron lifetime (τ) *vs*. time (during potential relaxation). All these plots are for a $CuWO_4$ electrode in an N_2 purged 0.2 M KPi buffer solution.

20. IPCE and APCE

The IPCE was calculated according to Eq. S13:

$$\mathrm{IPCE} = \frac{1239.8\ (\mathrm{V\ nm})\ j_{\mathrm{ph}}(\mathrm{mA\ cm^{-2}})}{\mathrm{P_{light}}(\mathrm{mW\ cm^{-2}})\ \lambda(\mathrm{nm})} \quad \text{(S13)}$$

IPCE can be related to the efficiencies of the different processes involved in the photoresponse:

$$\mathrm{IPCE} = \eta_{e^-/h^+}\eta_{transport}\eta_{interface} \quad \text{(S14)}$$

where λ is the wavelength, j_{ph} is the measured photocurrent density at a specific λ, P_{light} is the power of the monochromatic light at a given λ, η_{e^-/h^+} is the fraction of incident photons that are absorbed, giving rise to electron/hole pairs, $\eta_{transport}$ is the charge transport efficiency within the electrode, and $\eta_{interface}$ is the interfacial charge transfer efficiency.

The absorbed photon-to-current efficiency (APCE) is calculated according to Eq. S15:

$$\mathrm{APCE} = \frac{\mathrm{IPCE}}{A_\lambda} \quad \text{(S15)}$$

APCE can be

$$\mathrm{APCE} = \frac{\mathrm{IPCE}}{\eta_{e^-/h^+}} = \eta_{transport}\eta_{interface} \quad \text{(S16)}$$

where A_λ is the absorptance at a certain λ.

The short-circuit current density (J_{SC}) can be obtained from the IPCE measurements according to Eq. S17:

$$J_{SC} = \int_{\lambda_2}^{\lambda_1} e \cdot \mathrm{IPCE}(\lambda) \cdot E(\lambda) \cdot \frac{\lambda}{h \cdot c} \cdot d\lambda \quad (17)$$

being e the elementary charge ($1.60 \cdot 10^{-19}$ C), E(λ) the spectral irradiance (AM1.5G solar spectrum, W m^{-2} nm^{-1}), λ the wavelength (nm), h the Planck's constant ($6.63 \cdot 10^{-34}$ J s), and c the speed of light (m s^{-1}).

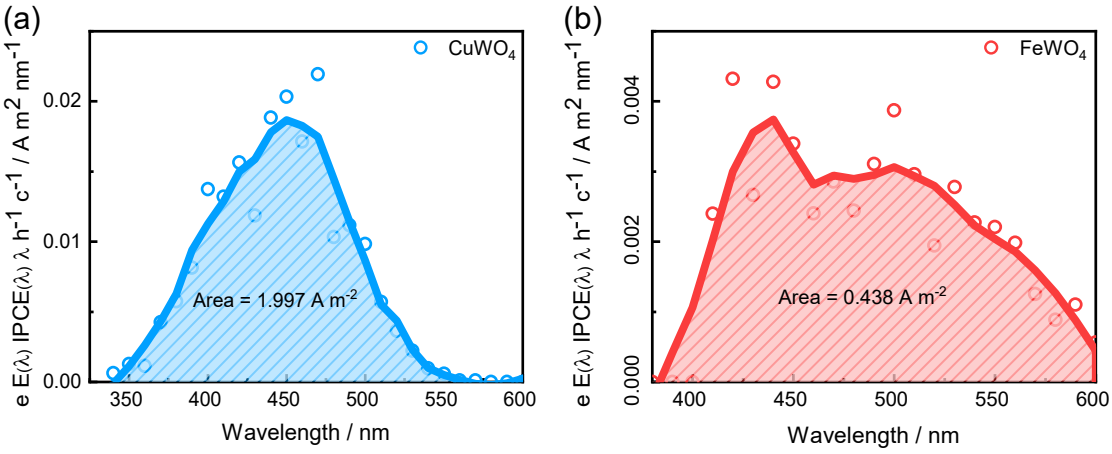

Figure S17. Short-circuit photocurrent density from IPCE values for a) $CuWO_4$ and b) $FeWO_4$.

21. Chronoamperometry at different pH values

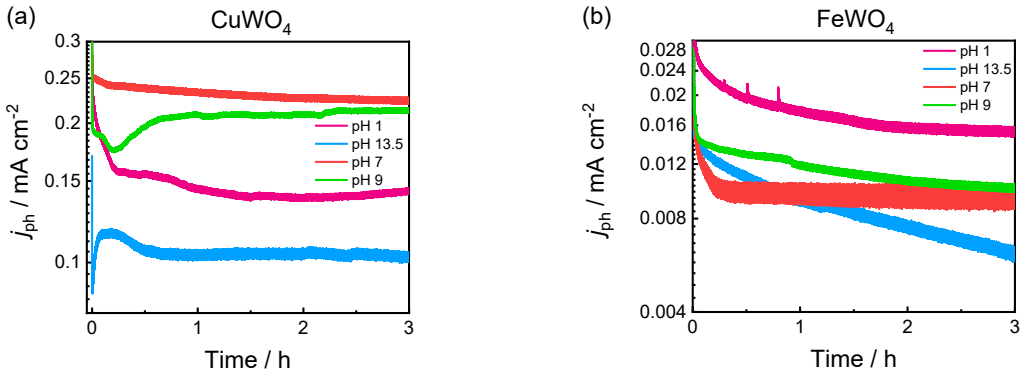

Figure S18. Chronoamperometric curves for $CuWO_4$ and $FeWO_4$ electrodes at 1.23 V_{RHE} for different media: 0.1 M H_2SO_4 (pH 1), 0.1 M KOH (pH 13.5), 0.2 M KPi (pH 7), and 0.1 M KBi (pH 9). *KBi stands for buffer borate, and KPi for buffer phosphate.

10. Bibliography

1 G. K. H. Madsen, J. Carrete and M. J. Verstraete, *Comput Phys Commun*, 2018, 231, 140–145.

2 D. Monllor-Satoca, L. Borja, A. Rodes, R. Gómez and P. Salvador, *ChemPhysChem*, 2006, 7, 2540–2551.

3 Y. A. Sethi, A. K. Kulkarni, A. A. Ambalkar, S. K. Khore, A. R. Gunjal, S. W. Gosavi and B. B. Kale, *Nanoscale Adv*, 2021, 3, 508–516.

4 L. Li, Y. Li, Y. Li, H. Ye, A. Lu, H. Ding, C. Wang, Q. Zhou, J. Shi and X. Ji, *Chem Geol*, 2021, 575, 120253.

5 V. Rathi, A. Panneerselvam and R. Sathiyapriya, *Journal of Materials Science: Materials in Electronics*, 2020, 31, 14823–14837.

6 M. Assis, A. C. M. Tello, F. S. A. Abud, P. Negre, L. K. Ribeiro, R. A. P. Ribeiro, S. H. Masunaga, A. E. B. Lima, G. E. Luz, R. F. Jardim, A. B. F. Silva, J. Andrés and E. Longo, *Appl Surf Sci*, 2022, 600, 154081.

7 P. Mal, P. Rambabu, G. R. Turpu, A. K. Gupta, B. Chakraborty, P. Sen and P. Das, *AIP Conf Proc*, 2016, 1728, 020323.

8 D. Kong, X. Hu, J. Geng, Y. Zhao, D. Fan, Y. Lu, W. Geng, D. Zhang, J. Liu, H. Li and X. Pu, *Appl Surf Sci*, 2022, 591, 153256.

9 Q. Gao and Z. Liu, *Progress in Natural Science: Materials International*, 2017, 27, 556–560.

10 K. Buvaneswari, R. Karthiga, B. Kavitha, M. Rajarajan and A. Suganthi, *Appl Surf Sci*, 2015, 356, 333–340.

11 R. Schuler, F. Bianchini, T. Norby and H. Fjellvåg, *ACS Appl Mater Interfaces*, 2021, 13, 7416–7422.

12 M. Jeyakanthan, U. Subramanian and R. B. Tangsali, *Journal of Materials Science: Materials in Electronics*, 2018, 29, 1914–1924.

13 P. Chatterjee and A. K. Chakraborty, *Solar Energy*, 2022, 232, 312–319.

14 S. Sagadevan, J. Podder and I. Das, *Journal of Materials Science: Materials in Electronics*, 2016, 27, 9885–9890.

15 E. Bandiello, P. Rodríguez-Hernández, A. Muñoz, M. B. Buenestado, C. Popescu and D. Errandonea, *Mater Adv*, 2021, 2, 5955–5966.

16 E. S. Babu, B. J. Rani, G. Ravi, R. Yuvakkumar, R. K. Guduru, V. Ganesh and S. Kim, *Mater Lett*, 2018, 220, 209–212.

17 S. M. AlShehri, J. Ahmed, A. M. Alzahrani and T. Ahamad, *New J. Chem.*, 2017, 41, 8178–8186.

18 M. Zhang, P. Tan, L. Yang, H. Zhai, H. Liu, J. Chen, R. Ren, X. Tan and J. Pan, *J Colloid Interface Sci*, 2023, 634, 817–826.

19 T. Zhu, M. N. Chong, E. S. Chan and J. D. Ocon, *J Alloys Compd*, 2018, 762, 90–97.

20 S. Shepard and M. Smeu, *Comput Mater Sci*, 2018, 143, 301–307.

21 A. Sarwar, A. Razzaq, M. Zafar, I. Idrees, F. Rehman and W. Y. Kim, *Results Phys*, 2023, 45, 106253.

22 Y. Cui, C. Lin, M. Li, N. Zhu, J. Meng and J. Zhao, *J Alloys Compd*, 2022, 893, 162181.

23 L. Chen, W. Li, W. Qiu, G. He, K. Wang, Y. Liu, Q. Wu and J. Li, *ACS Applied Materials & Interfaces*, 2022, 14, 47737–47746.

24 P. Raizada, S. Sharma, A. Kumar, P. Singh, A. A. Parwaz Khan and A. M. Asiri, *J Environ Chem Eng*, 2020, 8, 104230.

25 L. Zhen, Z. Yulian, L. Wen, C. Chunxu and Z. Jinfeng, *Mater Sci Semicond Process*, 2023, 160, 107445.

26 M. Dai, Z. He, P. Zhang, X. Li and S. Wang, *J Mater Sci Technol*, 2022, 122, 231–242.

27 Y. Wu, J. Zhang, B. Long and H. Zhang, *ACS Omega*, 2021, 6, 15057–15067.

28 D. Meziani, Y. Roumila, N. Y. Ghoul, D. Benmeriem, K. Abdmeziem and M. Trari, *Journal of Solid State Electrochemistry*, 2021, 25, 2097–2106.

29 X. M. C. Ta, T. K. A. Nguyen, A. D. Bui, H. T. Nguyen, R. Daiyan, R. Amal, T. Tran-Phu and A. Tricoli, *Adv Mater Technol*, 2023, 8, 2201760.

30 P. K. Pandey, N. S. Bhave and R. B. Kharat, *J Mater Sci*, 2007, 42, 7927–7933.

31 L. Fan, J. Sunarso, X. Zhang, X. Xiong, L. He, L. Luo, F. Wang, Z. Fan, C. Wu, D. Han, N. H. Wong, Y. Wang, G. Chen and W. Chen, *Int J Hydrogen Energy*, 2022, 47, 20153–20165.

32 J. U. Lee, J. H. Kim, K. Kang, Y. S. Shin, J. Y. Kim, J. H. Kim and J. S. Lee, *Renew Energy*, 2023, 203, 779–787.

33 N. Zhang, D. Chen, B. Cai, S. Wang, F. Niu, L. Qin and Y. Huang, *Int J Hydrogen Energy*, 2017, 42, 1962–1969.

34 A. Hankin, F. E. Bedoya-Lora, J. C. Alexander, A. Regoutz and G. H. Kelsall, *J Mater Chem A Mater*, 2019, 7, 26162–26176.

35 M. A. Butler and D. S. Ginley, *J Electrochem Soc*, 1978, 125, 228.

36 M. J. dos S. Costa, A. E. B. Lima, E. P. Ribeiro, G. dos S. Costa, E. Longo, G. E. da Luz, L. S. Cavalcante and R. da S. Santos, *J Appl Electrochem*, 2023, 53, 1349–1367.

37 A. E. B. Lima, M. Assis, A. L. S. Resende, H. L. S. Santos, L. H. Mascaro, E. Longo, R. S. Santos, L. S. Cavalcante and G. E. Luz, *Journal of Solid State Electrochemistry*, 2022, 26, 997–1011.

38 K. Wang, L. Chen, X. Liu, J. Li, Y. Liu, M. Liu, X. Qiu and W. Li, *Chemical Engineering Journal*, 2023, 471, 144730.

39 Y. Liu, L. Chen, X. Zhu, H. Qiu, K. Wang, W. Li, S. Cao, T. Zhang, Y. Cai, Q. Wu and J. Li, *Journal of Electroanalytical Chemistry*, 2022, 924, 116859.

40 C. M. Tian, M. Jiang, D. Tang, L. Qiao, H. Y. Xiao, F. E. Oropeza, J. P. Hofmann, E. J. M. Hensen, A. Tadich, W. Li, D. C. Qi and K. H. L. Zhang, *J. Mater. Chem. A*, 2019, 7, 11895–11907.

41 D. Monllor-Satoca and R. Gómez, *The Journal of Physical Chemistry C*, 2008, 112, 139–147.

42 N. Guijarro, T. Lana-Villarreal and R. Gómez, *ChemPhysChem*, 2012, 13, 3589–3594.